https://ntrs.nasa.gov/search.jsp?R=20170003713 2019-08-29T23:34:13+00:00Z

On the secondary eyewall formation of Hurricane Edouard (2014)

Sergio F. Abarca*,
I. M. Systems Group
National Oceanic and Atmospheric Administration
National Weather Service
National Centers for Environmental Protection
Michael T. Montgomery
Naval Postgraduate School, Monterey, CA
Scott A. Braun
National Aeronautics and Space Administration/Goddard Space Flight Center
And

Jason Dunion
University of Miami/CIMAS - NOAA/AOML/Hurricane Research Division, Miami, FL

---

*Corresponding author address: Sergio F. Abarca, mail: sergio.abarca @noaa.gov

Abstract

A first observationally-based estimation of departures from gradient wind balance during secondary eyewall formation is presented. The study is based on the Atlantic Hurricane Edouard (2014). This storm was observed during the National Aeronautics and Space Administration's (NASA) Hurricane and Severe Storm Sentinel (HS3) experiment, a field campaign conducted in collaboration with the National Oceanic and Atmospheric Administration (NOAA). A total of 135 dropsondes are analyzed in two separate time periods: one named the *secondary eyewall formation* period and the other one referred to as the *decaying-double eyewalled storm* period. During the secondary eyewall formation period, a time when the storm was observed to have only one eyewall, the diagnosed agradient force has a secondary maxima that coincides with the radial location of the secondary eyewall observed in the second period of study. The maximum spin up tendency of the radial influx of absolute vertical vorticity is within the boundary layer in the region of the eyewall of the storm and the spin up tendency structure elongates radially outward into the secondary region of supergradient wind, where the secondary wind maxima is observed in the second period of study. An analysis of the boundary-layer averaged vertical structure of equivalent potential temperature reveals a conditionally unstable environment in the secondary eyewall formation region. These findings support the hypothesis that deep convective activity in this region contributed to spin up of the boundary layer tangential winds and the formation of a secondary eyewall that is observed during the *decaying-double eyewalled storm* period.

1) Introduction

Secondary eyewalls are structures concentric to the primary eyewall of tropical cyclones and are characterized by maxima in tangential winds and convective activity. Given their frequency of occurrence (Hawkins and Helveston 2004, 2008; Kuo et al. 2008), their relationship with intensity change (e.g. Willoughby 1982; Houze et al. 2007; Yang et al. 2013), their association with longer duration of higher storm intensity (Kuo et al 2009) and their linkage to storm growth (Maclay et al. 2008), there is great interest in developing secondary eyewall forecasting tools. Today, the valuable and sophisticated forecasting tools tend to rely on empirical relationships (e.g. Kossin and Sitkowski 2009) and do not necessarily directly incorporate the physical processes of secondary eyewall formation.

Secondary eyewall formation dynamics have been the subject of intense contemporary research and contrasting views of the azimuthally averaged dynamics prevail. One line of thought suggests that the boundary layer contributes to the formation of secondary eyewalls by its participation in a feedback between a local enhancement of the radial vorticity gradient above the boundary layer, a corresponding frictional updraft and increased convective intensity (Kepert 2013). This view is based on the conception that linearized idealizations of the boundary layer of the hurricane inner core are useful representations of the dynamics of such regions of the storm (Kepert 2001; Kepert and Wang 2001). In this view, supergradient winds are a result of the existence of eyewalls and not precursors of them.

Another view of the role of boundary layer dynamics in secondary eyewall formation envisions the Eliassen axisymmetric balanced vortex dynamics being an appropriate framework to describe secondary eyewall formation and evolution (e.g. Zhu and Zhu 2012). In this view, proposed initially by Shapiro and Willoughby (1982), the boundary layer plays a role only as a sink of tangential momentum. In this model, the boundary layer acts to spin down the tangential wind in the layer. Studies, like that of Rozoff et al. 2012, focus on the balanced aspects of the problem.

In contrast with the two foregoing lines of thought, another perspective suggests that nonlinear boundary layer dynamics are essential to secondary eyewall formation and evolution (Huang et al. 2012; Abarca and Montgomery 2013; Abarca and Montgomery 2014). Huang et al. (2012) proposed that secondary eyewall formation is a progressive process that begins with a broadening of the tangential winds above the boundary layer, which is then followed by an increase of boundary layer inflow and amplification of the tangential wind in the boundary layer. The radial region of strong boundary layer convergence is associated with the generation of supergradient winds in and just above the boundary layer. These supergradient winds act in the radial momentum equation to arrest the inflow and cause a vertical eruption of moist air out of the boundary layer. In this model, the rising moist air will induce deep convection if the local environment supports convective instability.

The foregoing views highlight distinct and largely incompatible physical processes in the secondary eyewall formation problem. Despite their contrasting nature, these views have been invoked recently as acting simultaneously in a positive feedback process (e.g. Sun et al. 2013). In the current debate regarding the essential role of boundary layer dynamics in secondary eyewall formation a key point is *the existence of supergradient winds prior to the presence of the secondary eyewall itself.*

While most secondary eyewall studies have been based on numerical evidence, some are based on observations. Remote-sensing observational data of secondary eyewalls using various satellite microwave channels have resulted in useful knowledge of their frequency of occurrence around the world (e.g. Kuo et al. 2009; Yang et al. 2013). *In-situ* observations of secondary eyewalls have confirmed, *inter alia*, the existence of supergradient flow in the secondary eyewall (Didlake and Houze 2011; Bell et al. 2012). Using a model-derived dataset based on observations collected during the Tropical Cyclone Structure-2008 (TCS-08) field experiment (Elsberry and Harr, 2008), Huang et al. (2012) suggested that secondary eyewalls can be potentially predicted by diagnosing supergradient flow during secondary eyewall formation. To the knowledge of the authors, there has not been an attempt to assess the existence of supergradient flow in the boundary layer and its potential ramifications during secondary eyewall formation. In the light of the foregoing discussion, it is scientifically relevant to investigate the role of the boundary layer in supporting the formation of secondary eyewalls.

In the remainder of this article, we examine the secondary eyewall event of Hurricane Edouard (2014). Our emphasis is on the formation period of Eduoard’s secondary eyewall as captured jointly by in-situ observations made during the 2014 phase of the

National Aeronautics and Space Administration's (NASA) Hurricane and Severe Storm Sentinel (HS3) experiment (Braun et al. 2015) and Intensity Forecasting Experiment (IFEX, Rogers et al. 2013) research flights by the Hurricane Research Division of the National Oceanic and Atmospheric Administration (NOAA). Section 2 details the data and methodologies applied in the analysis of this work. Section 3 describes the synoptic evolution of Hurricane Edouard. Section 4 presents the scientific findings of this study. Section 5 offers conclusions and recommendations.

2) Summary of Hurricane Edouard (2014)

Figure 1 shows the track, maximum 1-min sustained surface winds, and minimum surface pressure of Edouard, as reported by the Best-Track dataset (Jarvinen et al. 1984). The storm developed from a tropical wave accompanied by a broad low pressure system and disorganized deep convection. The system was designated a tropical depression on 11 September and maintained a northwestward motion (Figure 1) for five days as it moved around the southwestern periphery of a subtropical ridge. Slow, but steady, strengthening occurred while the cyclone moved northwestward, with the system becoming a tropical storm on 12 September, a hurricane on 14 September, and a major hurricane on 16 September. Based on HS3 and satellite observations Braun et al. (2016) documented storm intensity and structural changes between 15 UTC 14 September and 09 UTC 15 September. The intensity changes included significant intensification before 00 UTC 15 September and weakening afterwards. They also included evidence of asymmetric eyewall convection and the existence of a larger eye at the end of the period than at its beginning. At 1500 UTC 14 September the storm exhibited strong winds in the northeastern quadrant (their Figure 4a), including an asymmetric secondary wind maxima. The radius of maximum winds was ~25 km and the secondary wind maxima was located ~50 km from the center of the storm. At 1315 UTC 15 September 2014 (their Fig. 3f) the eye had a radius about 4-5 times larger than seen earlier (their Fig. 3c). The authors interpreted such evolution as a possible eyewall replacement cycle, although as they show, there is no evidence of a concentric wind and precipitation maxima and at that time, and the storm was a Category 1 in the Saffir-Simpson scale.

Based on microwave satellite imagery [85/91 GHz brightness temperatures of 180-225 K (red to yellow shading) in the inner 150 km of the storm), Figure 1 shows observational evidence that Edouard evolved from a storm with a single eyewall on 15 September to one with a secondary eyewall on 17 September. The aircraft-borne data (as shown in upcoming sections) suggest that a secondary eyewall formed between these observation periods. For this reason, the time interval spanning the first set of observations will be referred to as the secondary eyewall formation period. After reaching its peak intensity (on 16 September), Edouard weakened quickly at a rate of 20 m s^{-1} per day.

The eyewall replacement cycle that took place, along with cold upwelling/mixing (of about 7°C (Stewart 2014, their Figure 5), were likely factors involved in the initial weakening of Edouard's maximum intensity. The vertical wind shear had a magnitude of 5-9 m s^{-1} (Figure 1) for most of the intensification period of the storm and during the first 6 hours of its weakening. At the time of its peak intensity, the storm changed its movement from northwestward to northeastward ahead of an approaching mid-latitude through. After the initial 6 hours of weakening, the vertical wind shear magnitude dropped relatively rapidly, and it then slowly increased over the following two days up to a value of 17 m s^{-1} on 19 September as the storm became embedded in the mid-latitude westerlies. On 19 September, Edouard was downgraded to a tropical storm and on 21 September, it merged with a frontal system (Stewart, 2014).

3) Data and methodology

The data used in this study consists of GPS dropsondes deployed from the unmanned Global Hawk as part of the HS3 campaign (Wick 2015) and the NOAA G-IV jet and WP-3Ds as part of the NOAA IFEX program, the National Hurricane Center (NHC)–Tropical Prediction Center (TPC) Best-Track dataset, the Statistical Hurricane Intensity Prediction Scheme (SHIPS) 200-850 hPa vertical wind-shear analyses (DeMaria and Kaplan, 1994; DeMaria and Kaplan, 1999; and DeMaria et al., 2005) and 85/91 GHz microwave satellite imagery from the Defense Meteorological Satellite Program (DMSP) microwave imagers [Special Sensor Microwave Imager (SSM/I; F-15) and the Special Sensor Microwave Imager/ Sounder (SSMIS; F-18)].

This study focuses on two study periods defined by the dropsonde availability. The first study period is referred to hereafter as the *secondary eyewall formation period*. This period uses 48 GPS dropsondes deployed from the NOAA research missions on 15 Sep between 14:13 UTC and 19:20 UTC. The flights are NOAA 42 (13 GPS dropsondes; while 14 GPS dropsondes were deployed, the 1802 UTC drop had no altitude information and was not included in this study), NOAA 43 (19 GPS dropsondes) and NOAA 49 (16 GPS dropsondes). The GPS dropsondes during the secondary eyewall formation period were deployed at about 700 hPa pressure altitude, which roughly corresponds to 3-km height.

The second period of study is referred to hereafter as the *decaying double eyewalled storm*. It includes 87 GPS dropsondes (Black et al. 2011) deployed from the Global Hawk at altitudes of ~17-19 km during the period from 16 Sep 1506 UTC to 17 Sep 0828 UTC. While three NOAA research missions deployed 52 GPS dropsondes between 16 Sep 1357 UTC and 17 Sep 1656 UTC (i.e. within our second period of study), these GPS dropsondes were mostly deployed in the south-southwest region of the storm. This quadrant of the storm was characterized by inflow throughout the troposphere (not shown) and is not representative of the azimuthal averages aimed in this study (see below). As a result, these NOAA GPS dropsondes deployed on 16-17 Sep are not included in this work.

The Best Track tropical cyclone latitude, longitude, and intensity (originally every 6 hours) were linearly interpolated to a temporal frequency of 10-minutes. The 10-minute storm center was then used to determine the storm-relative location of GPS dropsondes throughout their descent. Figure 2 shows the radial and azimuthal locations of all GPS dropsondes relative to the center of the storm. Note in the figure the homogeneity of the azimuthal distribution of the dropsondes and the high density of data within 400 km from the storm center. The dropsondes are also well distributed in the observation periods with about 10 GPS dropsondes per hour in the secondary eyewall formation period and about 5 dropsondes per hour in the decaying double-eyewalled storm period.

The secondary eyewall formation period spans 5 hours. This unprecedented observational density of the phenomena offers a unique opportunity to capture essentially a snap shot of the storm's processes resulting in the secondary eyewall. The decaying double-eyewalled storm observation period spanned 18 hours. During this time the inner core of the storm evolved substantially as the eyewall replacement was taking place, and here the observations are not to be interpreted as a snap shot of the storm, but rather diagnosing the processes that were ongoing during the 18 hours.

The GPS dropsonde wind and pressure/temperature/humidity observations have a frequency of 4 Hz and 2 Hz respectively and were interpolated to a uniform vertical grid with 301 points with 50 m of distance between grid points. This choice of vertical resolution represents a reduction of resolution from the original ~10 m. Such reduction does not impact the conclusions of this study. The lowest point was chosen at 10 m height and highest point was chosen at 15,010 m. Each GPS dropsonde profile interpolated to the fixed vertical grid was assigned to a radial bin according to the radial location of its deployment. In this work, it is assumed that the storm is axisymmetric enough to get estimates of the azimuthal averages of the different variables by averaging all GPS dropsondes available in a given radial bin. The radial bins are uniformly distributed using a subjective criterion as a compromise between number of radial bins and number of GPS dropsondes in each bin. For the secondary eyewall formation period, the radial bins are centered at 8.7, 22.5, 32.5, 48.8, 69.6, 101.0 ,150.0, 212.5, and 305.0 km radius (Figures 4-6) and for the decaying double-eyewalled storm the radial bins are centered at 5.0, 16.3, 31.3, 51.3, 76.3, 121.3, 188.8, 255.0, 322.5, 400.0, 475.0, 550.0 and

720.0 km (Figure 3). While GPS dropsondes drift radially as they descend through the troposphere, such displacements are smaller than the radial length of the bins considered in this study. The results discussed here are robust to data being assigned to radial bins using their individual radius, irrespective of the dropsonde they belong to. The data is also robust to different bin-length choices (not shown).

The quantities reported by the GPS dropsondes used in this study are height[1], horizontal wind velocities, pressure, temperature and relative humidity. We present results of composite (azimuthally averaged) quantities derived as described above, of (storm-relative) radial and tangential velocities, relative humidity and the following quantities: radial vorticity flux $-u\zeta_a$ (where $\zeta_a = \partial v / \partial r + v / r + f$ is the azimuthally averaged absolute vertical vorticity, r is the radial distance, v is the azimuthally averaged tangential velocity, and f the Coriolis parameter at the latitude of the measurement, equivalent potential temperature θ_e, as defined by the Bolton formula (Bolton 1982), and the *agradient force per unit mass*, as defined by Smith *et al.* (2009):

$$AF = -\frac{1}{\rho}\frac{\partial p}{\partial r} + \frac{v^2}{r} + fv$$

where the indicated variables have their usual meaning, ρ is the azimuthally averaged density (computed with the equation of state), and p is the azimuthally averaged pressure. The centrifugal and Coriolis forces are computed at every measurement location, then interpolated to the vertical grid and finally composited, similar to the other

---

[1] Using geopotential height renders plots virtually indistinguishable from those presented here (not shown).

quantities, into the radial bins introduced above. The radial derivatives (e.g. pressure gradient in the computation of the agradient force) are computed as centered differences, based on the radial grid introduced above. One-sided centered differences are used in the first and last radial grid points.

4) Results

Figure 3 shows the estimated azimuthal average tangential velocity during the double-eyewalled storm period along with the radial location of the GPS dropsondes as discussed in Section 2. The tangential velocity exhibits a deep cyclonic circulation extending through the troposphere to an altitude in excess of 15 km within 100 km radius. The cyclonic circulation extends outwards to approximately 600 km and is surrounded by an anticyclonic circulation confined to the upper troposphere between 200 km and 500 km and that deepens with increasing radius beyond 500 km. The dropsonde analysis reveals two maxima in the tangential wind field. The inner maximum is located in the radial bin centered at 31.3 km radius. The outer maximum is located in the radial bin centered near 100 km radius. These wind maxima are approximately superposed with convective maxima in the storm, as evidence by microwave imagery (e.g. Figure 1). This combined evidence establishes the existence of a secondary eyewall in the second period of observation.

Figures 4 and 5 show the composite analysis during the secondary eyewall formation period. The figures include the radial location of the dropsondes in the analysis (Section 2) and focus on the lower troposphere below 3 km within 310 km radius of the storm center. This focus enables one to examine the physical processes of secondary eyewall formation in the boundary layer, the region containing the tangential wind maxima in both the primary and secondary eyewalls. Figure 4a shows the composite tangential velocity. This variable reaches its maximum (of roughly 60 m s^{-1}) at 310-m altitude and 25-km radius. At all altitudes observed in the domain, the tangential wind decreases monotonically with radius beyond the radius of maximum tangential wind and there is no evidence of a secondary wind maximum. Along with the satellite imagery corresponding to 15 Sep (Figure 1), the data demonstrate the one-eyewall configuration of the storm at the time of the analysis.

Figure 4b shows the composite agradient force during the secondary eyewall formation period. As expected, the agradient force in the outer region of the domain is relatively weak and negative i.e. the force is directed radially inward. Because the pressure gradient is essentially independent of height in the boundary layer, the inward directed agradient force is a reflection of the frictional reduction of the tangential wind and related reduction of the (outwardly directed) centrifugal and Coriolis forces. In the inner region of the vortex, the agradient force has two distinct regions of positive values. A positive agradient force implies that the tangential winds are supergradient. A positive agradient force in the boundary layer is dynamically important because it acts to arrest the inflow and influences where the air ascends into the vortex interior. In the presence of a convectively unstable environment, air lifted out of the boundary layer can reach its level of free convection and result in deep convective activity.

One of the regions of positive agradient force corresponds to the eyewall of the storm.

This region roughly extends radially from 10 to 65 km radius. This region of supergradient flow exhibits a maximum agradient force of several hundred m s^{-1} hr^{-1}. Large values of agradient force are expected in the boundary layer of the primary eyewall (Smith et al. 2009, Kepert and Wang 2011) of the storm and have been shown to extend vertically upwards several kilometers (e.g. Abarca and Montgomery 2014).

There is a second region of positive agradient force that is distinct from that of the primary eyewall. This region of supergradient flow roughly extends from 90 to 150 km radius (Fig. 4b). The maximum agradient force in this region surpasses 20 m s^{-1} hr^{-1}. Within the constraints of the radial and temporal sampling of the data, the secondary maxima in agradient force coincides with the radial location of the secondary eyewall observed in the second period of observation of this study, as discussed above (Figure 3a). The secondary maximum in the agradient force occurs before the secondary tangential wind maximum is observed. The existence of this secondary agradient force maximum supports the hypothesis that the processes of secondary eyewall formation are underway.

Figure 5 shows the estimated azimuthally averaged radial flow, absolute vorticity, and radial vorticity flux. The azimuthally averaged radial flow is characterized by large inflow at the lowest levels, with inflow larger than 2 m s^{-1} below about 1-km height. This layer of strong inflow is due primarily to the agradient force (Smith *et al.*, 2009; Bui *et al.*, 2009). In the analyzed grid (lowest vertical level at 10 m and 50 m vertical grid spacing), the vertical location of the inflow maxima increases with radius, going from 10 m to about 110 m height. The low elevation of the inflow maxima is consistent with fluid dynamical considerations for a swirling-flow boundary layer (e.g. Bo Dewadt, 1940;

Schlichting, 1968, chapter 11) and with observations of a mature hurricane (e.g. Montgomery et al. 2014). In the domain, there are two extended regions of outflow. One corresponds to the eyewall of the storm, located above 700-m height, between 30- and 70-km radius. Within the analysis domain, the outflow reaches its maximum at 2.3 km height in the radial bin centered near 50-km radius. The other extended region of outflow is roughly located between 85- to 170-km radius and between about 1.7- and 2.1-km height.

Figure 5b shows the estimated azimuthally averaged absolute vorticity. In the inner core of mature tropical cyclones, this field is generally characterized by a central region of large vorticity surrounded by a skirt of smaller values (Mallen et al. 2005). Not withstanding the limitations of the data, the overall vorticity structure is as expected, with the largest values in the innermost points. The absolute vorticity structure includes a monotonic decrease of vorticity with radius above 1-km height. The field exhibits no discernable relative maxima of vorticity near the top of the boundary layer. Near 211 km radius, there is a small relative maximum in vorticity below 1 km.

Figure 5c shows the estimated mean radial absolute vertical vorticity flux (hereafter radial vorticity flux), as it appears in the right hand side of the tangential momentum equation (with a minus sign, see Eq. 4 in Abarca and Montgomery 2013). Radial vorticity flux is a key diagnostic of whether the secondary eyewall formation process is underway at the time analyzed. We present radial vorticity flux as it can be directly interpreted as a term in the tangential tendency equation, but we note here that such a quantity only differs from the radial advection of absolute angular momentum by a factor of r. From the perspective of the azimuthally averaged system-scale flow, the radial vorticity flux is one of the dominant terms in the tangential tendency equation during spinup of tropical cyclones in general (Ooyama 1969, Willoughby 1995, Smith et al. 2009), and during secondary eyewall formation in particular (e.g. Abarca and Montgomery 2013, their Figure 5). The maximum spin up tendency of the vorticity flux is within the boundary layer in the region of the eyewall of the storm and it elongates radially outward into the secondary region of supergradient wind where the secondary wind maxima is observed in the second period of study. Note that while the secondary eyewall formation is underway, there is no evidence of a vorticity bump above the boundary layer (Figure 5b) to support the idea that secondary eyewall formation is a feedback process that begins once a local vorticity maximum is present above the boundary layer (Kepert 2013, Kepert and Nolan 2014).

To gain additional insight into the relevant physical processes in the boundary layer of the storm during this early period of study, we calculate the vertical average of radial inflow. Collapsing the data in this way helps highlight the bulk features of the storm's boundary layer as it is undergoing secondary eyewall formation. Figure 6a shows the storm-relative radial velocity averaged below 1 km height (the results here after are not dependent on the choice of height, they are robust to other choices, like 0.8, 0.9 and 1.2 km, not shown). As suggested by Figure 5a, this height is chosen as the nominal depth of the boundary layer as it contains the region of relatively strong inflow. Figure 6a shows that, at the time of the analysis, the radial inflow depicts a structure with two maxima. The primary inflow maximum is at the radial bin centered near 30 km radius and is associated with the primary eyewall. The secondary inflow maximum is located at the radial bin centered near 100 km radius. It can be shown that the double inflow maximum structure cannot be explained by an argument based on frictional stress alone. The secondary inflow maximum can be explained plausibly by the action of the positive agradient force shown in Figure 4b around the interval centered near 100-km radius. As discussed above, this force field acts to arrest the inflow and promote ascent of moist air out of the boundary layer.

Figure 6b shows the composite vertical profile of the equivalent potential temperature (θ_e) and the corresponding saturated equivalent potential temperature (θ_{es}) at the radial bin centered near 100 km radius. The figure depicts a conditionally unstable environment in the secondary eyewall formation region. As an example, if one vertically averages θ_e in the lowest 200 m, this renders a mean value of 349.6 K. A parcel lifted from 100 m with such a θ_e would acquire positive buoyancy above about 1-km height (e.g., Holton 2004). Thus, this thermodynamic structure is capable of supporting deep convective activity in the radial region of secondary eyewall formation.

Conclusions

Secondary eyewall formation (SEF) dynamics have been the subject of intense contemporary research and contrasting views of the SEF azimuthally averaged dynamics prevail. In an effort to help provide an improved understanding of the physical processes controlling the formation of secondary eyewalls in real storms, we presented herein an estimation of azimuthally-averaged dynamical and thermodynamical fields derived from in-situ observations during SEF. The case study is that of Atlantic Hurricane Edouard

(2014). This storm was intensely observed during the 2014 phase of the NASA HS3 experiment, in conjunction with NOAA IFEX research flights by the Hurricane Research Division. A total of 135 GPS dropsondes were analyzed. The GPS dropsondes were deployed in two time periods: one named the *secondary eyewall formation* period (48 dropsondes deployed on 14 Sep within 5 hours) and the other one referred to as the *decaying-double eyewalled storm* period (87 GPS–dropsondes deployed on 16-17 Sep within 18 hours).

During the period designated as the secondary eyewall formation period, the estimates of azimuthally-averaged fields reveal that the storm had a single tangential wind maximum. During the double eyewall storm period, the azimuthally-averaged wind data confirmed a double tangential wind maximum, with the tangential wind maxima located within the boundary layer of the storm. During the secondary eyewall formation period, the agradient force had a secondary maxima that coincided with the radial location of the secondary eyewall observed in the second period of study. The storm-relative radial velocity averaged below 1 km height depicted a structure with two maxima, with the secondary inflow maximum coinciding with the radial location of the secondary eyewall observed in the second period of study. The maximum spin up tendency of the radial influx of absolute vertical vorticity was within the boundary layer in the region of the eyewall of the storm and it elongated radially outward into the secondary region of supergradient wind, where the secondary wind maxima was observed in the second period of study. An analysis of the average vertical structure of potential temperature revealed a conditionally unstable environment in the secondary eyewall formation region.

The evidence presented supports the hypothesis that secondary eyewall formation is underway during the first period of observations and the underlying mechanisms at work are in line with the dynamical and thermodynamical processes as articulated in Smith et al. (2009) and Huang et al. (2012).

The vertical coherence of the azimuthally-averaged estimates (using the 2-4 Hz GPS dropsonde observations interpolated to a regular vertical grid with spacing of 50 m) and the robustness of the results to radial bin choices suggest that the data presented herein is physically meaningful and useful.

In the light of the results presented, it is scientifically desirable from the operational point of view to investigate the role of the boundary layer in supporting the formation of secondary eyewalls in other observational cases. Analogous estimates of the quantities examined here in other storms are recommended to assess the generality of the results.

Acknowledgements

The first author gratefully acknowledges the support from the National Research Council (NRC) through its Research Associateship Program; the host institution, the Naval Postgraduate School (NPS) in Monterey; California and Scott Braun for the funding that made it possible for him to participate in the HS3 deployment during the 2014 hurricane season. MTM acknowledges the support of NSF grant AGS-1313948, NOAA HFIP grant

N0017315WR00048, NASA HS3 grant NNG11PK021, and the U.S. Naval Postgraduate School.

References

Abarca, S. F., and M. T. Montgomery, 2013: Essential dynamics of secondary eyewall formation. J. Atmos. Sci., 70, 3216–3230, doi:10.1175/JAS-D-12-0318.1.

Abarca, S. F., and M. T. Montgomery, 2014: Are Eyewall Replacement Cycles Governed Largely by Axisymmetric Balance Dynamics? J. Atmos. Sci., 72, 82-87, doi: http://dx.doi.org/10.1175/JAS-D-14-0151.1

Bell, M. M., M. T. Montgomery and W. C. Lee, 2012b: An axisymmetric view of concentric eyewall evolution in Hurricane Rita (2005). J. Atmos. Sci., 69, 2414–2432.

Black, M. L., G. A. Wick, J. R. Spackman, T. Hock, and R. Hood, 2011: Real-time data transmission, processing and dissemination of GPS dropwindsonde data from the NASA Global Hawk unmanned aircraft. 2011 Fall Meeting, San Francisco, Calif., Amer. Geophys. Union, 5-9 Dec.

Bödewadt, U. T., 1940: Die Drehströmung übder fester Grund. Z. Angew, Math. Mech., **20**, 241-253.

Bolton, D., 1980: The computation of equivalent potential tem- perature. Mon. Wea. Rev., 108, 1046–1053.

Braun, S. A., P. A. Newman, and G. M. Heymsfield, 2015: NASA's Hurricane and Severe Storm Sentinel (HS3) Investigation. *Bull. Amer. Meteor. Soc.*, (submitted).

Bui, H. H., R. K. Smith, M. T. Montgomery, and J. Peng, 2009: Balanced and unbalanced aspects of tropical-cyclone in- tensification. Quart. J. Roy. Meteor. Soc., 135, 1715–1731.

DeMaria, M., and J. Kaplan, 1994: A statistical hurricane intensity prediction scheme (SHIPS) for the Atlantic basin. *Wea. Forecasting,* **9,** 209–220.

DeMaria, M., and J. Kaplan, 1999: An updated statistical hurricane intensity prediction scheme (SHIPS) for the Atlantic and eastern North Pacific basins. *Wea. Forecasting,* **14,** 326–337.

DeMaria, M., M. Mainelli, L. K. Shay, J. A. Knaff, and J. Kaplan, 2005: Further Improvements to the Statistical Hurricane Intensity Prediction Scheme (SHIPS). *Wea. Forecasting*, **20**, 531–543.

Didlake, A. C., Jr., and R. A. Houze Jr., 2011: Kinematics of the secondary eyewall observed in Hurricane Rita (2005). J. At- mos. Sci., 68, 1620–1636.

Elsberry, R. L., and P. A. Harr, 2008: Tropical Cyclone Structure (TCS08) field experiment science basis, observational platforms, and strategy. Asia-Pacific J. Atmos. Sci., 44, 209–231.

Hawkins, J. D., and M. Helveston, 2004: Tropical cyclone multiple eyewall characteristics. *Preprints of the 26th Cnference on Hurricanes and Tropical Meteorology,* Amer. Meteor. Soc., Miami, FL, 3-7 May, 276–277.

Hawkins, J. D., and M. Helveston, 2008: Tropical cyclone multiple eyewall characteristics. *28th Conference on Hurricanes and Tropical Meteorology,* Amer. Meteor.

Soc., Orlando, FL, 28 April – 2 May.

Holton, J. R., 2004: An Introduction to Dynamic Meteorology. Elsevier Academic, 535 pp.

Houze, R. A. J., S. S. Chen, B. F. Smull, W. C. Lee, and M. M. Bell, 2007: Hurricane intensity and eyewall replacement. Science, 315, 1235–1239, doi:10.1126/science.1135650.

Huang, Y.-H., M. T. Montgomery, and C.-C. Wu, 2012: Concentric eyewall formation in Typhoon Sinlaku (2008). Part II: Axi- symmetric dynamical processes. J. Atmos. Sci., 69, 662–674, doi:10.1175/JAS-D-11-0114.1.

Jarvinen, B. R., C. J. Neumann, and M. A. S. Davis, 1984: A tropical cyclone data tape for the North Atlantic basin, 1886–1983: Contents, limitations, and uses. NOAA Tech. Memo. NWS NHC 22, 21 pp.

Kepert, J. D., 2013: How does the boundary layer contribute to eyewall replacement cycles in axisymmetric tropical cyclones? J. Atmos. Sci., 70, 2808–2830, doi:10.1175/JAS-D-13-046.1.

Kepert, Jeffrey D., and David S. Nolan, 2014: Reply. J. Atmos. Sci., 71, 4692-4704.

Kepert, J. D., and Y. Wang, 2001: The dynamics of boundary layer jets within the tropical cyclone core. Part I: Linear theory. *J. Atmos. Sci.,* **58**, 2469–2484.

Kossin, J. P., and M. Sitkowski, 2009: An objective model for identifying secondary eyewall formation in hurricanes. *Mon. Wea. Rev.*, **137**, 876–892.

Kuo, H.-C., C.-P. Chang, Y.-T. Yang, and H.-J. Jiang, 2009: Western North Pacific typhoons with concentric eyewalls. *Mon. Wea. Rev.*, **137**, 3758–3770.

Kuo, H.-C., W. H. Schubert, C.-L. Tsai, and Y.-F. Kuo, 2008: Vortex interactions and barotropic aspects of concentric eyewall formation. *Mon. Wea. Rev.*, **136**, 5183– 5198.

Maclay, K. S., M. DeMaria, and T. H. Vonder Haar, 2008: Tropical cyclone inner core kinetic energy evolution. *Mon. Wea. Rev.*, **136**, 4882–4898.

Mallen, K. J., M. T. Montgomery, and B. Wang, 2005: Reexamining the near-core radial structure of the tropical cyclone primary circulation: Implications for vortex resiliency. *J. Atmos. Sci.*, **62**, 408–425.

Montgomery, M.T., J. A. Zhang, and R. K. Smith, 2014: The low-level structure of rapidly intensifying and mature Hurricane Earl (2010). *Quart. J. Roy. Meteor. Soc.,* **140**, 2132-2146.

Ooyama, K.V. 1969. Numerical simulation of the life cycle of tropical cyclones. *J. Atmos. Sci., 26*, 3–40.

Rogers, R.F., S.D. Aberson, A. Aksoy, B. Annane, M. Black, J.J. Cione, N. Dorst, J. Dunion, J.F. Gamache, S.B. Goldenberg, S.G. Gopalakrishnan, J. Kaplan, B.W. Klotz, S. Lorsolo, F.D. Marks, S.T. Murillo, M.D. Powell, P.D. Reasor, K.J. Sellwood, E.W. Uhlhorn, T. Vukicevic, J.A. Zhang, and X. Zhang, 2913: NOAA’s Hurricane Intensity Forecasting Experiment (IFEX): A progress report. *Bull. Amer. Meteor. Soc*., **94 (6)**, 859-882.

Rozoff, C. M., D. S. Nolan, J. P. Kossin, F. Zhang, and J. Fang, 2012: The roles of an expanding wind field and inertial stability in tropical cyclone secondary eyewall formation. J. Atmos. Sci., 69, 2621–2643, doi:10.1175/JAS-D-11-0326.1.

Schlichting, H., 1968: Boundary layer theory (6th edn.). McGraw-Hill: New York, N.Y.

Smith, R. K., M. T. Montgomery, and N. Van Sang, 2009: Tropical cyclone spin-up revisited. Quart. J. Roy. Meteor. Soc., 135, 1321–1335, doi:10.1002/qj.428.

Stewart, S. R., 2014: Tropical Cyclone Report, Hurricane Edouard 11-19 September 2014. Tropical Cyclone Report, National Hurricane Center 19pp.

Shapiro, L. J., and H. E. Willoughby, 1982: The response of bal- anced hurricanes to local sources of heat and momentum. J. Atmos. Sci., 39, 378–394, doi:10.1175/1520-0469(1982)039,0378: TROBHT.2.0.CO;2.

Sun, Y. Q., Y. Jiang, B. Tan, and F. Zhang, 2013: The governing dynamics of the secondary eyewall formation of Typhoon Sinlaku (2008). J. Atmos. Sci., 70, 3818–3837, doi:10.1175/JAS-D-13-044.1.

Wick, Gary. 2015. Hurricane and Severe Storm Sentinel (HS3) Global Hawk AVAPS Dropsonde System. Dataset available online [https://hs3.nsstc.nasa.gov/pub/hs3/AVAPS/] from the NASA Global Hydrology Resource Center DAAC, Huntsville, Alabama, U.S.A. doi: http://dx.doi.org/10.5067/HS3/AVAPS/DROPSONDE/DATA201.

Willoughby, H. E., J. A. Clos, and M. G. Shoreibah, 1982: Concentric eye walls, secondary wind maxima, and the evolution of the hurricane vortex. J. Atmos. Sci., 39, 395–411, doi:10.1175/1520-0469(1982)039,0395: CEWSWM.2.0.CO;2.

Yang, Y. T., H-C. Kuo, E. A. Hendricks, and M. S. Peng, 2013: Structural and Intensity Changes of Concentric Eyewall Typhoons in the Western North Pacific Basin. *Mon. Wea. Rev.*, **141**, 2632–2648.

Zhu, Z., and P. Zhu, 2014: The role of outer rainband convection in governing the eyewall replacement cycle in numerical simu- lations of tropical cyclones. J. Geophys. Res. Atmos., 119, 8049–8072, doi:10.1002/2014JD021899.

List of Figures

Figure 1. Edouard (2014) as captured by (upper left) DMSP F-15 SSM/I 85 GHz and (upper right) DMSP F-18 SSMIS 91 GHz microwave satellite imagery and the NHC-TCP best track dataset intensity and track (center and bottom panels). The period of study, between 09/16 15:06:37 UTC and 09/17 08:28:03 UTC is highlighted with solid thick lines. Also shown are the shear magnitude (blue line) and direction (green line), as captured by Statistical Hurricane Intensity Predictor Scheme (SHIPS).

Figure 2. Locations of dropsonde deployments, relative to the storm center, during a) the secondary eyewall formation period (9/15, from 14:13 to 19:20 UTC) and b) the mature and decaying secondary eyewall period (from 9/16 16:06 UTC to 9/17 08:28 UTC). The concentric circles indicate the radial distance (in km) from the center of the storm.

Figure 3. Composite a) tangential wind velocity (m s^{-1}), and b) radial location of the dropsondes for the decaying double eyewalled storm period. In the top panel a color bar is used to display the structure of tangential velocity. In the bottom panel the black dots indicate the average measurement radius for each dropsonde in the analysis (distributed in the vertical to avoid superposition). The red lines indicate the radial location of the center of the analysis bins. The bins are delimited by the locations of the vertical blue lines. The numbers superposed on the red lines indicate the number of dropsondes in each radial bin (see text for further details).

Figure 4. Composite a) tangential wind velocity (m s^{-1}), b) Agradient Force (m^2 s^{-1} hr^{-1}), and c) radial location of the dropsondes for the secondary eyewall formation period. In the two top panels the orange and red colors indicate increasingly

positive values, respectively; blue colors indicate negative values. In the bottom panel, the black dots indicate the average measurement radius for each dropsonde in the analysis. The red lines indicate the radial location of the center of the bins. The bins are delimited by the locations of the vertical blue lines. The numbers superposed on the red lines indicate the number of dropsondes in each radial bin (see text for further details).

Figure 5. Composite a) radial velocity (m s^{-1}), b) absolute vorticity (s^{-1} X 10^{-4}), and c) radial vorticity flux (m s^{1} hr^{-1}) for the secondary eyewall formation period. For a) and c) the color bar indicates increasingly positive values beginning with light brown through dark red; increasingly negative values are indicated with darker shades of blue. For b) the color bar indicates only positive values. (See text for further details.)

Figure 6. a) Vertically averaged (in the lowest km) radial flow as a function of radius, and b) Vertical profiles of equivalent potential temperature and saturated equivalent potential temperature (K). In the top panel, the vertical red lines indicate the radial location of the center of the bins. The bins are delimited by the locations of the vertical blue lines. The number superposed on the red lines indicates the number of dropsondes in each radial bin (see text for further details).

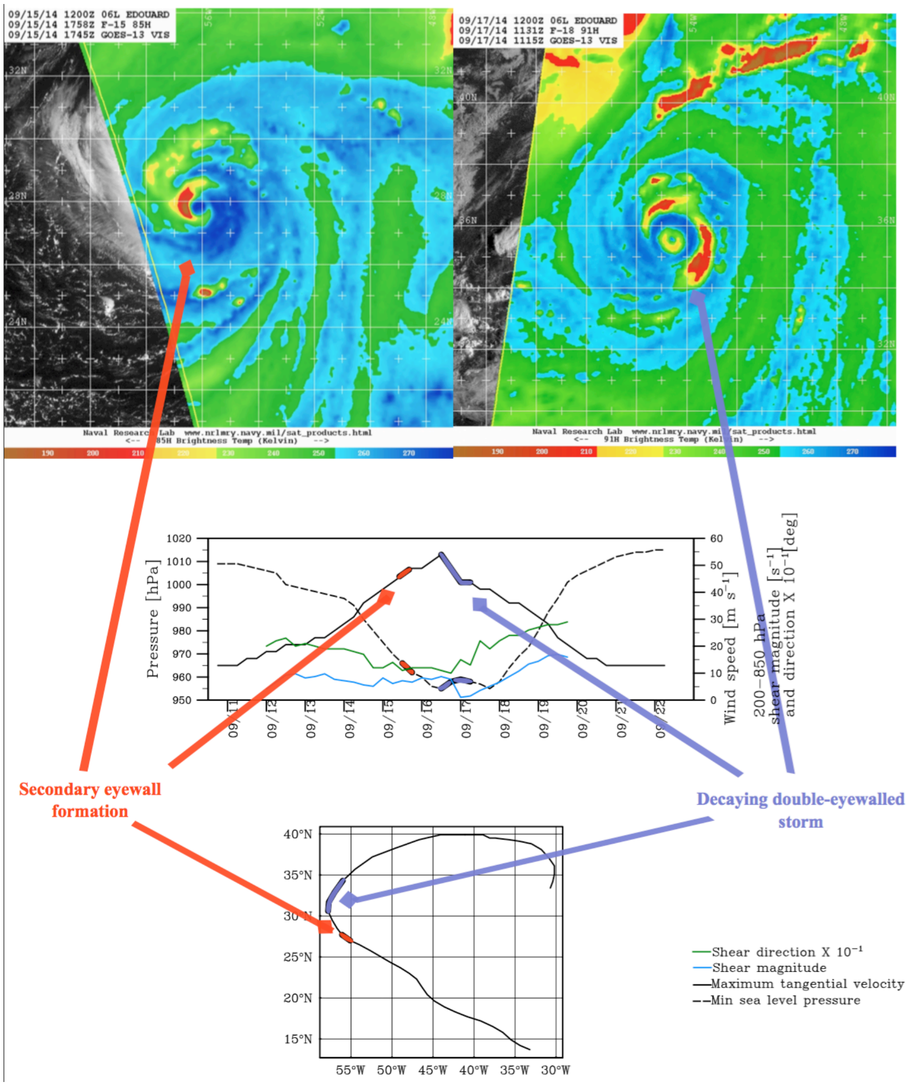

Figure 1. Edouard (2014) as captured by by (upper left) DMSP F-15 SSM/I 85 GHz and (upper right) DMSP F-18 SSMIS 91 GHz microwave satellite imagery and the NHC-TCP best track dataset intensity and track (center and bottom panels). The period of study, between 09/16 15:06:37 UTC and 09/17 08:28:03 UTC is highlighted with solid thick lines. Also shown are the shear magnitude (blue line) and direction (green line), as captured by Statistical Hurricane Intensity Predictor Scheme (SHIPS).

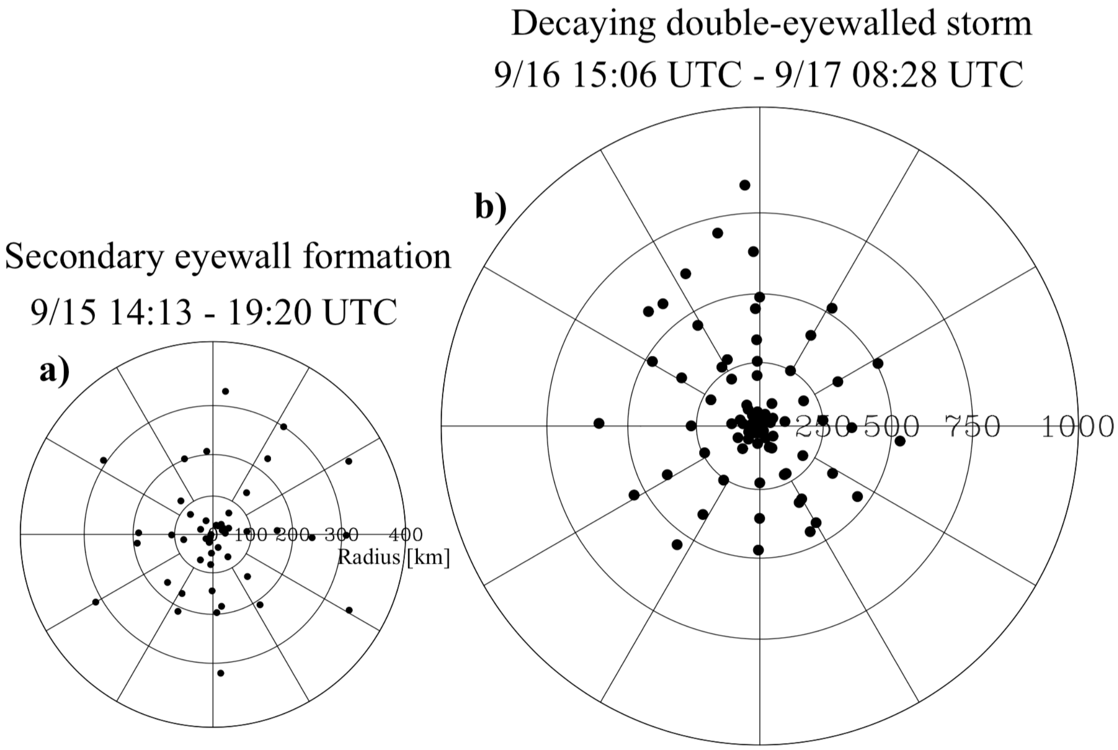

Figure 2. Locations of dropsonde deployments, relative to the storm center, during a) the secondary eyewall formation period (9/15, from 14:13 to 19:20 UTC) and b) the mature and decaying secondary eyewall period (from 9/16 15:06 UTC to 9/17 08:28 UTC). The concentric circles indicate the radial distance (in km) from the center of the storm. (Note: Horizontal scale in panel (a) is larger than scale in panel (b).)

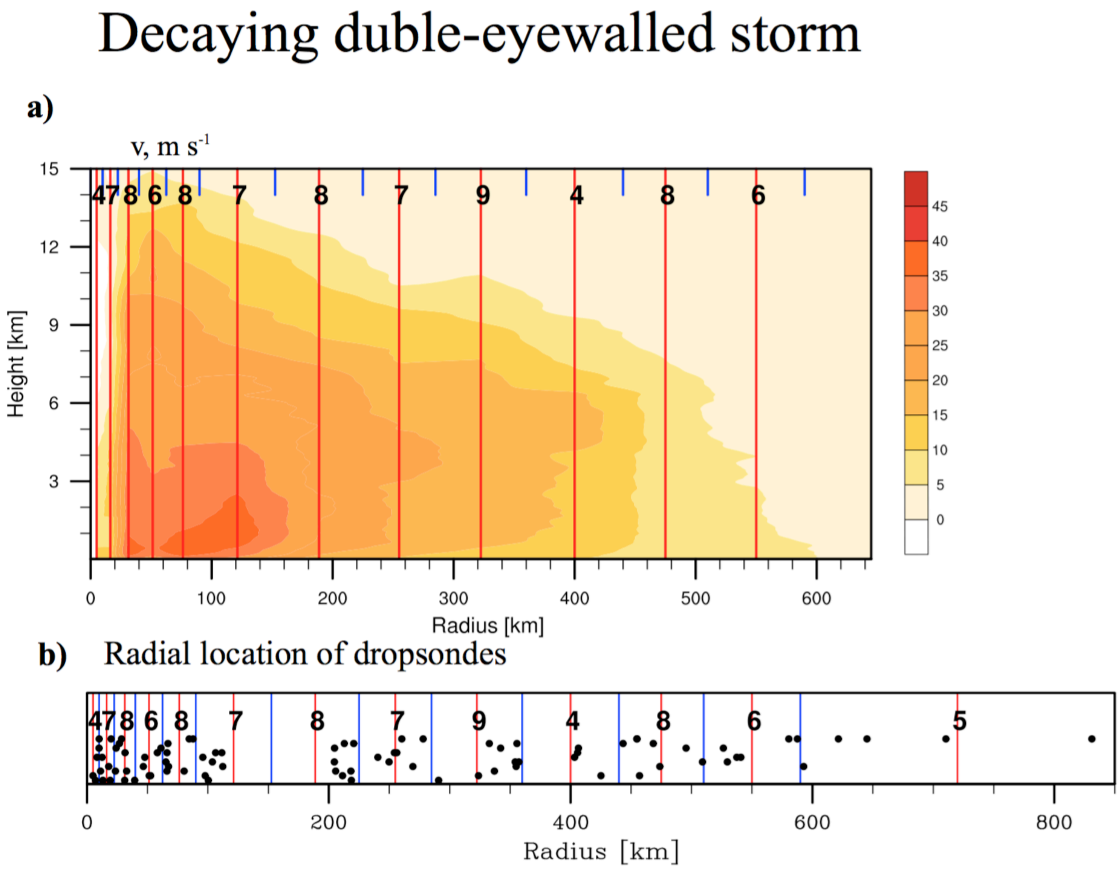

Figure 3. Composite a) tangential wind velocity (m s^{-1}), and b) radial location of the dropsondes for the decaying double eyewalled storm period. In the top panel a color bar is used to display the structure of tangential velocity. In the bottom panel the black dots indicate the average measurement radius for each dropsonde in the analysis (distributed in the vertical to avoid superposition). The red lines indicate the radial location of the center of the analysis bins. The bins are delimited by the locations of the vertical blue lines. The numbers superposed on the red lines indicate the number of dropsondes in each radial bin (see text for further details).

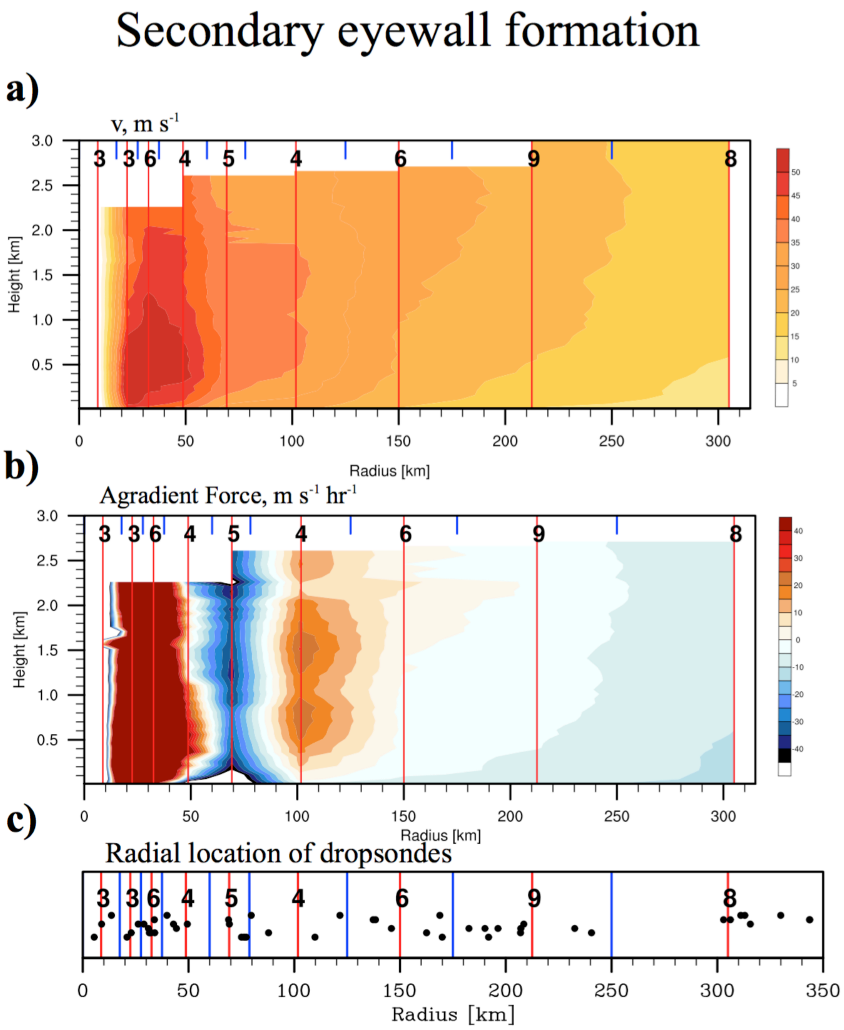

Figure 4. Composite a) tangential wind velocity (m s^{-1}), b) Agradient Force (m^2 s^{-1} hr^{-1}), and c) radial location of the dropsondes for the secondary eyewall formation period. In the two top panels the orange and red colors indicate increasingly positive values, respectively; blue colors indicate negative values. In the bottom panel, the black dots indicate the average measurement radius for each dropsonde in the analysis. The red lines indicate the radial location of the center of the bins. The bins are delimited by the locations of the vertical blue lines. The numbers superposed on the red lines indicate the number of dropsondes in each radial bin (see text for further details).

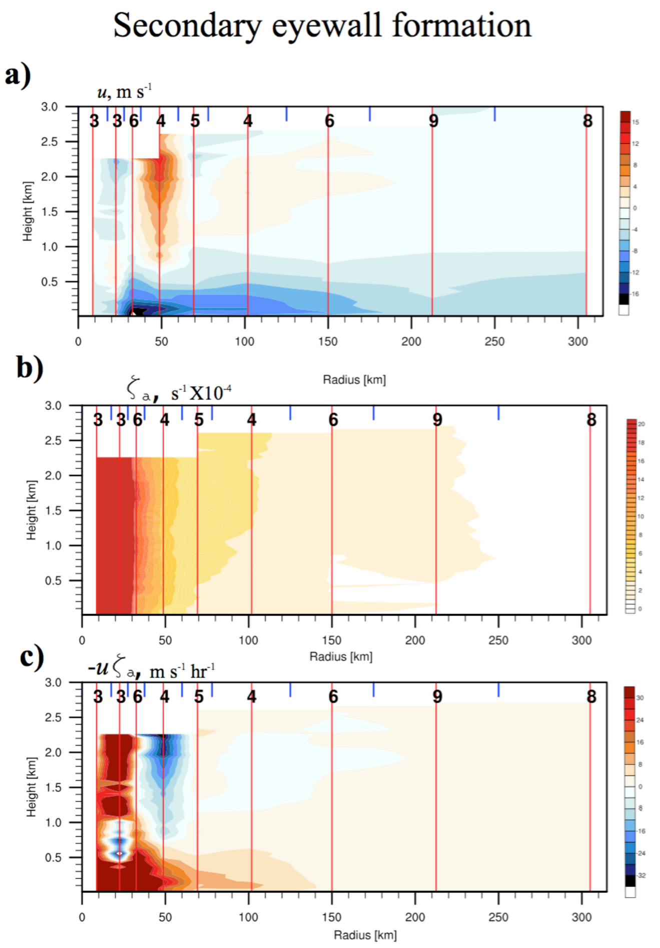

Figure 5. Composite a) radial velocity (m s^{-1}), b) absolute vorticity (s^{-1} X 10^{-4}), and c) radial vorticity flux (m s^{1} hr^{-1}) for the secondary eyewall formation period. For a) and c) the color bar indicates increasingly positive values beginning with light brown through dark red; increasingly negative values are indicated with darker shades of blue. For b) the color bar indicates only positive values. (See text for further details.)

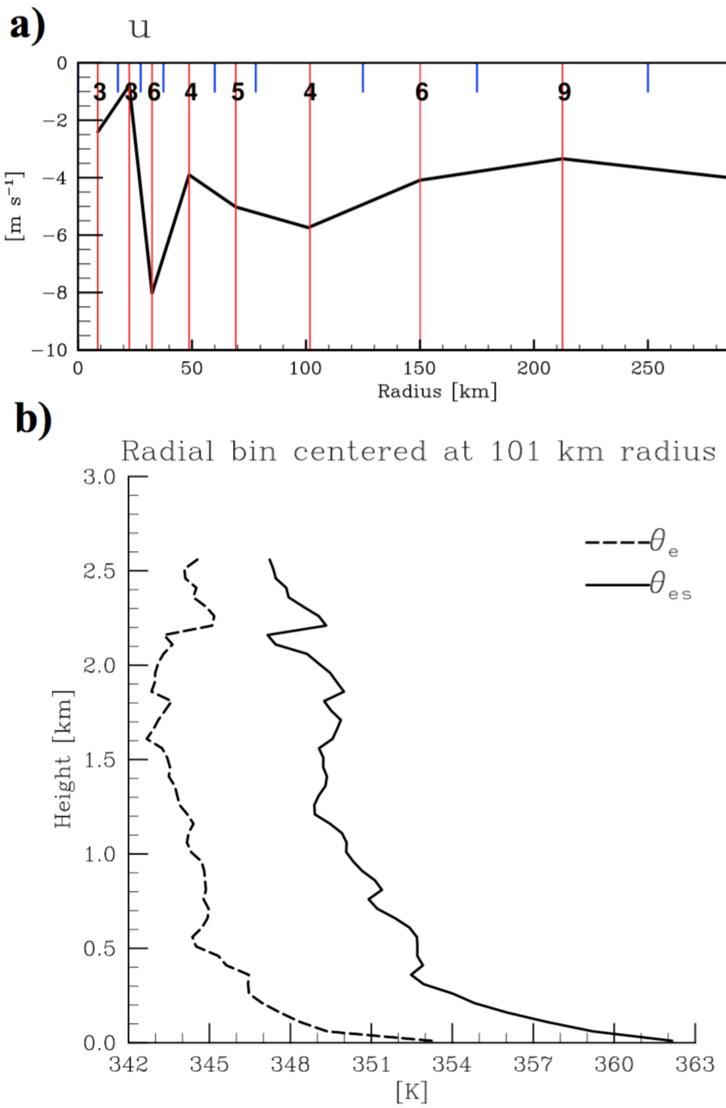

Figure 6. a) Vertically averaged (in the lowest km) radial flow as a function of radius, and b) Vertical profiles of equivalent potential temperature and saturated equivalent potential temperature (K). In the top panel, the vertical red lines indicate the radial location of the center of the bins. The bins are delimited by the locations of the vertical blue lines. The number superposed on the red lines indicates the number of dropsondes in each radial bin (see text for further details).